Wear 522 (2023) 204837

Contents lists available at ScienceDirect

Wear

journal homepage: www.elsevier.com/locate/wear

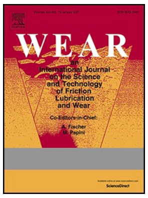

Identification of gear wear damage using topography analysis

J.C. Poletto [a,b,c,*], C.M.C.G. Fernandes [d], L.Y. Barros [a], P.D. Neis [a], K. Pondicherry [b,c], D. Fauconnier [b,c], J.H.O. Seabra [d], P. De Baets [b,c], N.F. Ferreira [a]

[a] Federal University of Rio Grande do Sul, Laboratory of Tribology, Osvaldo Aranha, 99, 90035-190, Porto Alegre, Brazil
[b] Ghent University, Soete Laboratory, Technologiepark Zwijnaarde 46, 9052, Zwijnaarde, Ghent, Belgium
[c] Flanders Make @ Ugent – Core Lab MIRO, Ghent, Belgium
[d] FEUP, Universidade do Porto, Rua Dr. Roberto Frias s/n, 4200-465, Porto, Portugal

ARTICLE INFO

Keywords:
Gears
Wear mechanism
Surface topography
Roughness parameters

ABSTRACT

Gear failure modes and their underlying mechanisms are usually identified by visual inspection, which relies on the skills and experience of the human observer and hence is prone to subjectivity and bias. Therefore, it is essential to design and implement objective methods to improve the identification of gear failure modes. In the present study, the 3D topography of gear surfaces affected by different types of wear modes, i.e., micropitting, pitting, and scuffing, was measured by means of white light interferometry. The surfaces were evaluated in terms of height, spatial, and function roughness parameters, according to ISO 25178-2. Besides, a new roughness parameter, named surface motion orientation (S_{mo}), was proposed. Three features were found relevant to identify the differences between the gear surfaces affected by different failure modes: the shape of asperities distribution, the severity of damage, and the surface texture orientation with respect to the motion direction. The combination of the roughness parameters selected to quantify each of these features (S_{sk}, S_q, S_{mo}) resulted in an objective classification of the assessed gear failure modes.

1. Introduction

Gears are critical components encountered in several industrial applications, such as automotive powertrains [1,2], aircraft engines [3], and wind turbines [4,5]. Gears are subjected to different types of wear during operation, which may lead to failure. The occurrence of a certain wear mechanism depends on several factors, including material, geometry, surface finishing, lubricant, and operating conditions. Micropitting, pitting, and scuffing are common types of gear failure modes [6–9].

Scuffing is the result of adhesive wear. The damage is inflicted on the gear flanks by repetitive welding and tearing of the opposing gear surface asperities and is directly correlated with the breakdown of the lubricant film [10–12]. Scuffing results in significant modification of the roughness of the gear surface [11]. A scuffed surface appears rough and plastically deformed, with bands of damage oriented in the sliding direction [12]. Pitting, on the other hand, is a contact fatigue failure mode that occurs due to cyclic loading of the gear surface under pure rolling or mixed rolling and sliding contact [12]. It is characterized by surface and subsurface fatigue cracks, which coalesce and grow to the surface, resulting in the detachment of material from the gear surface. Failure by pitting can be further categorized into distinguished failure modes: micropitting, macropitting and spalling, which are mainly differentiated by the size and severity of the damage.

Micropitting occurs under elastohydrodynamic (EHL) or mixed lubricating conditions. It is promoted by the propagation of surface cracks that results in the detachment of microscopic material fragments from the tooth surfaces [13–15]. Micropitting refers to pits of a few micrometers wide and 5–20 μm deep [12–14,16]. The most critical region for its occurrence is the zone below the pitch line, where the shear stresses due to sliding and rolling directions are opposite [13–18]. Although micropitting is not a catastrophic type of damage by itself, it may coalesce and further result in more severe types of failures, such as macropitting and spalling [9,12,13,19]. Macropitting is initiated by surface or nearby subsurface fatigue cracks [7,12]. These cracks propagates against the direction of the sliding force, resulting in the

---

[*] Corresponding author. Federal University of Rio Grande do Sul, Laboratory of Tribology, Osvaldo Aranha, 99, 90035-190, Porto Alegre, Brazil.

E-mail addresses: jean.poletto@ufrgs.br, jeancarlos.poletto@ugent.be, jeanpoletto@gmail.com (J.C. Poletto), cfernandes@fe.up.pt (C.M.C.G. Fernandes), liubarros@yahoo.com.br (L.Y. Barros), patric.neis79@gmail.com (P.D. Neis), KannakiShanmugham.Pondicherry@UGent.be (K. Pondicherry), Dieter.Fauconnier@UGent.be (D. Fauconnier), jseabra@fe.up.pt (J.H.O. Seabra), Patrick.DeBaets@UGent.be (P. De Baets), neyferr@gmail.com (N.F. Ferreira).

https://doi.org/10.1016/j.wear.2023.204837
Received 3 October 2022; Received in revised form 24 January 2023; Accepted 25 January 2023

detachment of material from the gear surface. Macropits appears as scattered and shallow pits up to 500 μm wide and usually between 30 and 90 μm deep [20]. Lastly, large spalls, also known as spalling, may develop due to the propagation of subsurface fatigue cracks, resulting in irregular craters that cover a significant area of the tooth flank [12,21].

Today, gear failure modes are still identified by visual inspection of the tooth flanks [7,22]. This method is costly, time-consuming, and rather subjective since it relies on an experienced material failure analyst to label the image according to standardized datasets, such as the ISO 10825 [12]. Moreover, even following strict standard guidelines, there is no guarantee that different analysts would label a certain damage as the same failure mode. Consequently, the development of classification tools based on objective metrics is valuable to improve robustness and reduce the subjectivity of the current approach. Only a limited amount of recent studies were found [22–25] which propose an automated classification system of wear mechanisms. These works are mainly focused on image analysis through machine learning techniques, such as convolutional neural networks [22], random forest [23], k-means clustering [24], and artificial neural networks [25]. From this set of studies, the study of Chang et al. [22] was the only one focused on gear failure modes. They analyzed microscopy images of gear replicas and designed a convolutional neural network able to categorize the images into four wear mechanisms: normal, abrasion, pitting, and scuffing. Based on the good results achieved (98% of accuracy), the authors concluded that this strategy has a high potential to automate the classification of gear wear mechanisms. Although they obtained replicas of the gear surfaces, the authors did not explore the topography content of these replicas and limited themselves to the investigation of the images taken from the replicas.

Nonetheless, as pointed out by Wolski et al. [24], the data contained in an image is the intensity of light reflected by the specimen and then captured by the camera sensor. Hence, the light intensity does not strictly and directly relate to the depth of the damage itself. Moreover, image acquisition is known to be affected by different aspects, such as sharpness and lighting conditions during photo exposure. Therefore, the topographical data of a damaged surface can provide valuable and more complete information about the type and severity of the wear mechanism. In this context, the same authors analyzed the surfaces of steel samples subjected to pin-on-plate reciprocating tests. Using fractal and curvature signatures of the surface topography, they were able to distinguish the wear mechanisms between adhesive, abrasive, and corrosive wear. As a result, the authors have shown that it is possible to use topography data to design an automated classification system of worn surfaces.

To the best of the authors' knowledge, there is still no literature that provides an objective classification of gear failure modes based on the topography data of the worn gear surfaces. Therefore, an in-depth analysis of different gear failure mode topography was carried out in this paper. The three-dimensional surface of gears previously subjected to standard micropitting, pitting, and scuffing FZG[1] gear tests were measured by white light interferometry. They were further evaluated in terms of height, spatial, and function roughness parameters, as per ISO 25178-2 [26]. Finally, the most adequate set of roughness parameters was identified to objectively classify distinct gear failure modes.

2. Methodology

2.1. Gear samples

Three sets of gears were assessed in this work. These gear sets had been previously evaluated on an FZG back-to-back gear test rig. The first gear set, composed of standard FZG A20 gear geometry with a 4.5 mm module, was subjected to the standard ISO 14635-1 FZG scuffing test method A/8.3/90 [27]. The second set was subjected to the DGMK-FZG-micropitting short test GFKT-C/8.3/90 [28]. Finally, the third set was subjected to the DGMK-FZG short-duration pitting test [29]. Both the second (micropitting) and the third (pitting) gear sets were composed of standard FZG type C14 gears, with a module of 4.5 mm. For detailed information about the FZG experimental procedures, please refer to the following literature: scuffing [11,30], micropitting [14,15], and pitting [18]. From each gear set, two gear teeth (6 teeth in total) were used for the assessment of the surface topography.

2.2. Surface measurements

The gear surfaces were digitally scanned using a Keyence VR-5200 optical profilometer and are shown in Figs. 1–3, for the scuffing, micropitting, and pitting gear sets, respectively. The areas highlighted in colored bounding boxes show the approximate position where the topography analysis was performed. The horizontal white dashed line in these figures indicate the position of the pitch line. For interpretation of the colors used in all figures of this manuscript, the reader is referred to the online version of this article. A Taylor Hobson CCI-HD white light interferometer was used to perform the topography measurements of the highlighted areas, except for the two large spalling defects (large red areas in Fig. 3), which were measured with the Keyence equipment. According to the equipment manufacturers, the Taylor Hobson CCI-HD can provide vertical resolution as good as 0.1 Å, while the Keyence VR-5200 is limited to a vertical resolution of 0.1 μm. In both equipment, the spatial resolution varies according to the magnification lens used during the measurement.

The surface of the gear set subjected to scuffing can be seen in Fig. 1. In both teeth, the scuffing marks covered the entire gear surface. The location and visual appearance of the scuffing marks are consistent with those reported in the literature [10,11,22]. The topography measurements were performed with the Taylor Hobson interferometer, using the 10 × magnification, which resulted in 0.83 μm of spatial resolution. To prevent a biased analysis, ten equally spaced and non-overlapping areas of 1.6 × 1.6 mm^2 were distributed over the gear surfaces. They are highlighted in Fig. 1 as blue bounding boxes above the pitch line.

The surface of the gear set subjected to micropitting tests is shown in Fig. 2. It is possible to notice the grey-stained area below the pitch line, near the tooth root. The location and aspect of the defect are consistent with the appearance of micropitting, as reported in the literature [6,7,12,15,17–19]. Due to the small size of the micropits, a magnification of 50 × was used in the Taylor Hobson interferometer, resulting in a spatial resolution of 0.165 μm. Ten equally spaced areas of 0.33 × 0.33 mm^2 were measured in the location, where micropitting was expected. These areas are highlighted in orange bounding boxes in Fig. 2.

In the surfaces of the pitting gear set, exhibited in Fig. 3, two failure modes were detected: macropitting and spalling. Several occurrences of macropitting defects are observed on the gear surface. They are scattered through the gear surface, predominantly in the same region where micropitting is observed on the first gear set. According to the literature [7,20], macropitting is initiated between the pitch line and the tooth root, after which it propagates towards and beyond the pitch line. Therefore, seven measurement areas, highlighted in small green bounding boxes in Fig. 3, were defined in this region. These measurements were performed with the Taylor Hobson equipment, using the same settings as for the scuffing evaluation, i.e. 10 × magnification, an area size of 1.6 x 1.6 mm^2, and 0.83 μm spatial resolution. On the other hand, two large spalling defects, highlighted in red bounding boxes, are observed on the gear flanks. Hence, two areas with 5.0 × 5.0 mm^2 and 3.0 × 3.0 mm^2 were defined for the assessment of the surface topography. Due to the large area and depth of these defects, the Keyence optical profilometer was employed, resulting in spatial resolution of 1.85 μm for both surfaces representative of the spalling failure mode.

The software Taylor Hobson TalyMap Platinum 6.2 was used for

---

[1] FZG (*Forschungsstelle für Zahnräder und Getriebebau*) denotes the Gear Research Center at the Technical University of Munich.

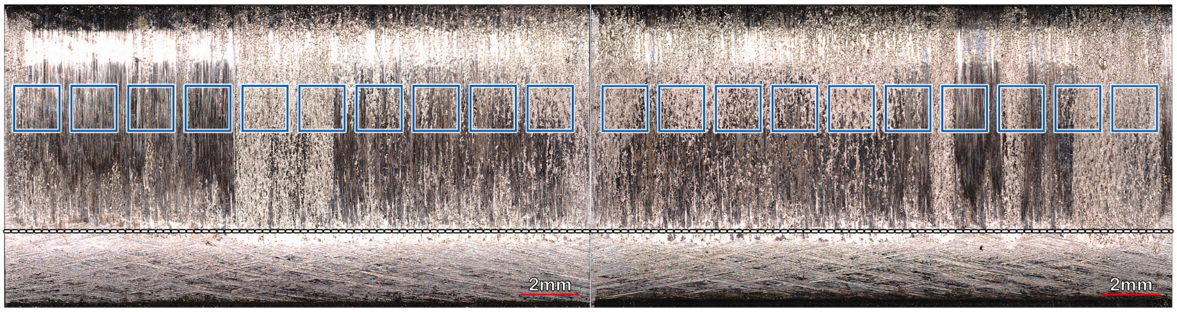

Fig. 1. Optical image of gears from scuffing tests, highlighted bounding boxes (blue) indicate where topography analysis was performed. (For interpretation of the references to color in this figure legend, the reader is referred to the Web version of this article.)

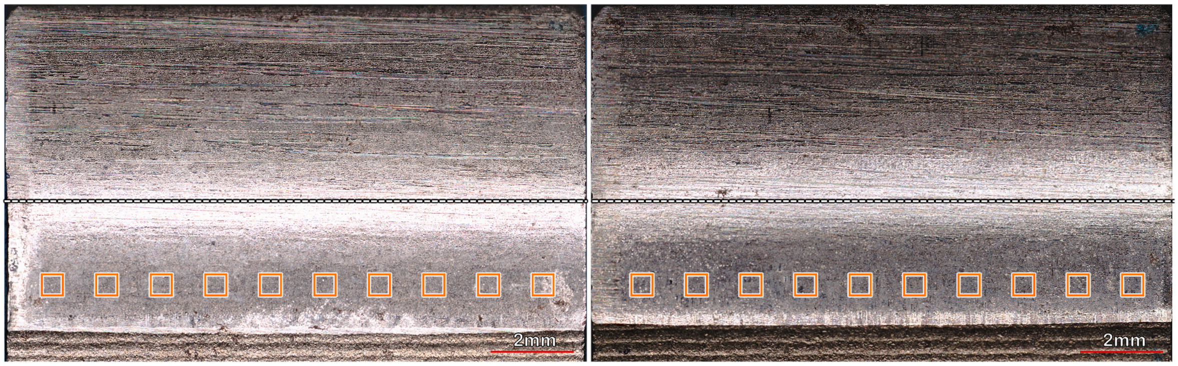

Fig. 2. Optical image of gear set from micropitting tests, highlighted bounding boxes (in orange) indicate where topography analysis was performed. (For interpretation of the references to color in this figure legend, the reader is referred to the Web version of this article.)

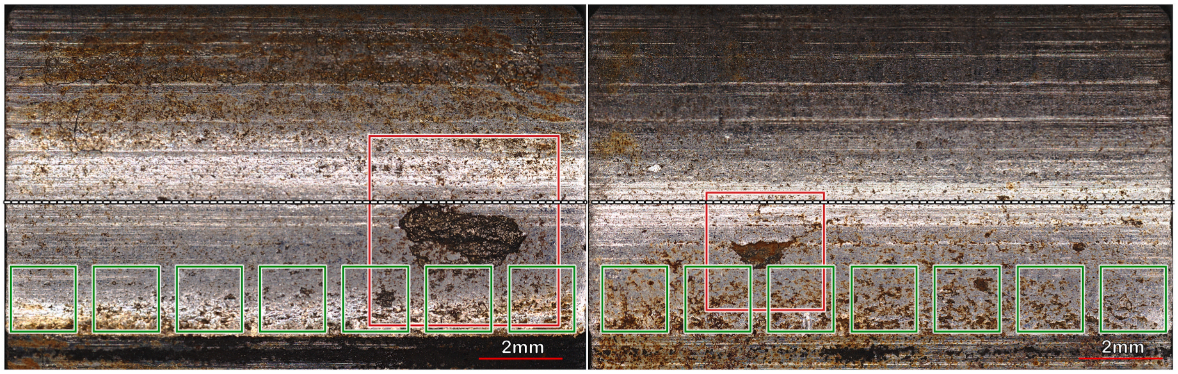

Fig. 3. Optical image of gears from pitting tests, highlighted bounding boxes (green for macropitting and red for spalling) indicate the location where topography analysis was performed. (For interpretation of the references to color in this figure legend, the reader is referred to the Web version of this article.)

filtering the measured surfaces and for quantification of the roughness parameters. First, the form was removed assuming a 2nd order polynomial approximation of the nominal surface. Then, outliers were removed by symmetrical probability trimming of 0.1% over the areal material ratio curve. Then, the remaining non-measured values were filled by averaging the nearest neighbors. Finally, the scale-limited surface was obtained by applying a robust gaussian regression filter between short (λ_s) and long (λ_c) wavelength cutoffs. Table 1 summarizes the measurement and filter settings for each type of surface topography evaluated.

Table 1
Measurement and filter settings of topography measurements for each failure mode.

Gear set	Failure mode	Amount of areas per gear set	Evaluated area size	Spatial resolution	Wavelength content of the scale-limited surface ($\lambda_s - \lambda_c$)
scuffing	scuffing	20	1.6 × 1.6 mm^2	0.83 μm	2.5 μm–800 μm
micropitting	micropitting	20	0.33 × 0.33 mm^2	0.165 μm	0.5 μm–250 μm
pitting	macropitting	14	1.6 × 1.6 mm^2	0.83 μm	2.5 μm–800 μm
pitting	spalling	2	3.0 × 3.0 mm^2 5.0 × 5.0 mm^2	1.85 μm	10 μm–2500 μm

2.3. Topography analysis

The filtered surfaces were evaluated in terms of height, function, and spatial categories of roughness parameters according to the standard ISO 25178-2 [26]. Height and function parameters have been traditionally employed for evaluating gear topography [11,13–15,18,31]. Moreover, spatial parameters were included in this investigation due to the necessity of evaluating how the damage is oriented with respect to the motion direction. An important remark regarding the physical meaning of the evaluated roughness parameters is presented herein: they can either indicate the shape of the asperities distribution, the severity of the damage, or how the defects are spatially distributed over the surface. These three features (shape, severity and spatial distribution) will further prove to be important to distinguish different gear failure modes. Table 2 relates the evaluated roughness parameters to the categories described in the standard ISO 25178-2 [26] and to the corresponding physical meaning.

The skewness (S_{sk}) and the kurtosis (S_{ku}) parameters are capable of indicating the shape of the asperity distribution. A graphical representation of the effect of both parameters over the asperities probability density function (PDF) is shown in Fig. 4. In this graph, the orange solid line represents the shape of a PDF that corresponds to a perfectly gaussian distributed, homogeneous isotropic roughness, resulting in $S_{sk} = 0$ and $S_{ku} = 3$. The skewness parameter indicates if the surface is asymmetrically distributed towards peaks ($S_{sk} > 0$) or valleys ($S_{sk} < 0$). Meanwhile, the kurtosis parameter is directly related to the degree of flatness of the surface.

The root mean square height (S_q) parameter and the arithmetical mean height (S_a) can be used to quantify the severity of damage. The S_q parameter and S_a are often used to provide a general description of the surface roughness. Both parameters (S_a and S_q) are strongly correlated with each other [32,33]. In comparison to S_a, the S_q parameter provides more relevant statistical meaning [33] and it is slightly more sensible to the height variations [34]. Therefore, only the S_q parameter was analyzed.

Furthermore, the function parameters (S_{pk}, S_k, S_{vk}), can also indicate the severity of the damage. These parameters are categorized as function parameters in ISO 25178-2 [26] because they are based on the cumulative distribution function (CDF), which can be obtained by integrating the PDF. The CDF of an asperity distribution is equivalent to the widespread nomenclatures of the areal material ratio function [26], bearing area ratio curve [35–37], and Abbott-Firestone curve [35,37,38]. To obtain the function parameters, an algorithm, detailed in the standard ISO 25178-2 [26], splits the CDF into three zones: peaks, core, and valleys. Each one of these zones is then associated with a roughness parameter: reduced peak height (S_{pk}), core height (S_k) and reduced valley height (S_{vk}), respectively. These parameters are graphically described in Fig. 5. Thereafter, these function parameters can indicate the scale of the asperities height in each specific portion of the surface: peaks (S_{pk}), core (S_k) or valleys (S_{vk}).

Table 2
Relation between the roughness parameters, their categories according to ISO 25178-2 [26], and their physical meaning.

Roughness parameter	Symbol	ISO 25178-2 category	Physical meaning
skewness	S_{sk}	height parameters	shape of the asperity distribution
Kurtosis	S_{ku}		
root mean square height	S_q		severity of damage
reduced peak height	S_{pk}	function parameters	
core height	S_k		
reduced dale height	S_{vk}		
texture aspect ratio	S_{tr}	spatial parameters	spatial orientation of the surface texture
texture direction	S_{td}	miscellaneous parameters	
surface motion orientation	S_{mo}	-	

Both height (S_{sk}, S_{ku}, S_q) and function (S_{pk}, S_k, S_{vk}) parameters are obtained solely based on the height data of the surface, and they do not take into consideration how the defects appear arranged over the surface. However, some references [13,39,40] had shown that this spatial distribution of the defects is relevant information to characterize the wear damage. Hence, the spatial and miscellaneous parameters' texture aspect ratio (S_{tr}) and texture direction (S_{td}), detailed in ISO 25178-2 [26], were used to better understand how the assessed failure modes are distributed over the surface.

The texture aspect ratio (S_{tr}) is defined as the ratio between the distances corresponding to the fastest and lowest decays of the surface autocorrelation function [26,41]. This parameter quantifies the strength of the texture uniformity, assuming values ranging from $S_{tr} = 0$ in case of anisotropic surfaces, to $S_{tr} = 1$ for isotropic surfaces. According to Blunt and Jiang [41], small values of the parameter (S_{tr} <0.3) indicates a strong directional surface. Meanwhile, larger values (S_{tr} >0.5) indicates an uniform texture in all directions. Additionally, the S_{tr} parameter alone does not provide any information about the direction of the anisotropy. To assess this feature of the surface, the S_{td} parameter is required.

The texture direction (S_{td}) is defined as the angle corresponding to the absolute maximum value of the surface angular spectrum [26]. It measures the most pronounced direction of the surface texture [41]. The possible values assumed by the S_{td} are between 0° and 180°. Nevertheless, the information provided by the S_{td} parameter is only relevant for anisotropic surfaces, since an isotropic surface does not have a pronounced direction. The same limitation was highlighted by Blunt and Jiang [41], who stated that the information provided by the S_{td} parameter is meaningless for highly isotropic surfaces (S_{tr} >0.5).

Considering the relationship between the S_{tr} and S_{td} parameters, Qi et al. [32] evaluated several machined surfaces and found a very weak ($| r_s | = 0.01$) Spearman's correlation between these parameters. Grabon and Pawlus [42] reported similar results ($|\rho| = 0.19$) when assessing Pearson's correlation between S_{tr} and S_{td} in the study of two-process surfaces. These results emphasize that both parameters (S_{tr} and S_{td}) contain independent and relevant information for the characterization of the surface topography. Meanwhile, it is necessary to evaluate these parameters simultaneously to obtain a complete understanding of how the texture features are spatially distributed over the surface.

Therefore, a new roughness parameter is proposed: the surface motion orientation (S_{mo}). The S_{mo} parameter was specially designed for the assessment of worn surfaces. It combines the S_{tr} and S_{td} parameters, according to Equation (1), resulting in a dimensionless parameter, which ranges from −1 to +1. The proposed parameter is capable of indicating the intensity and orientation of the surface texture with respect to the motion direction. The combination of these features resulted in a single indicator with stronger physical meaning if compared to the S_{tr} or S_{td} parameters treated individually.

$$S_{mo} = (1 - S_{tr})\cos(2(S_{td} - \theta_{\parallel})) \tag{1}$$

where S_{tr} is the texture aspect ratio [−], the S_{td} is the texture direction [°] and $\theta_{\parallel}$ is the direction of the motion [°].

To improve the understanding of the proposed parameter, Equation (1) can be separated into two terms, one to assess the contribution of the S_{tr} parameter and another to assess the contribution of the S_{td} parameter. The first term of the equation ($1 - S_{tr}$) is used to invert the relation provided by the texture aspect ratio (S_{tr}). Hence, the module of the S_{mo} parameter varies linearly according to the S_{tr} parameter, from $| S_{mo} | =$

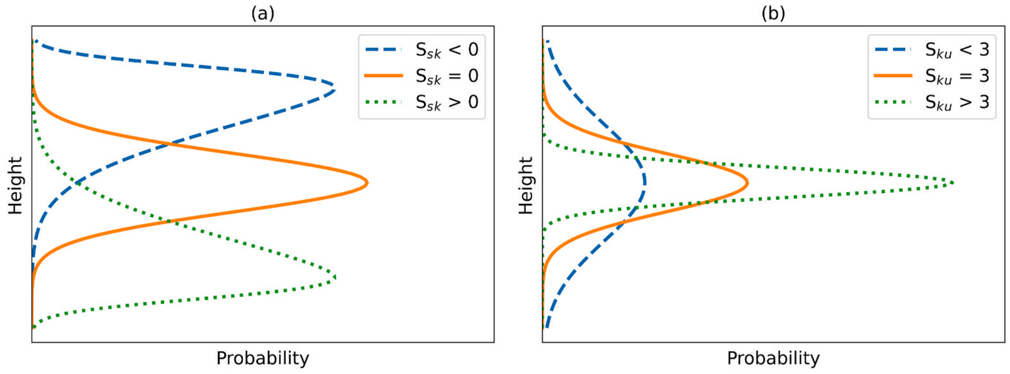

Fig. 4. Theoretical probability distribution functions (PDF) showing how the shape of the asperity distribution affects the values of skewness (a) and kurtosis (b) parameters.

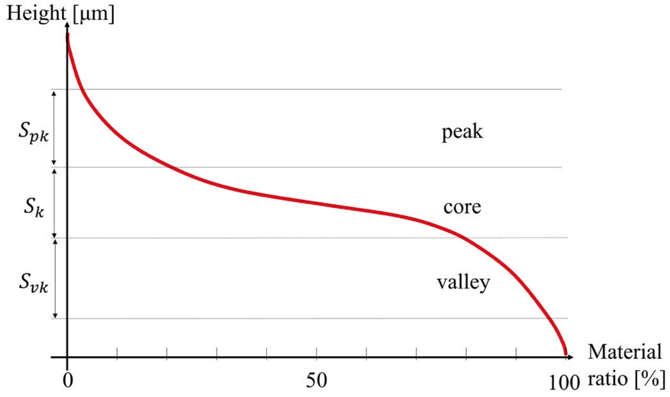

Fig. 5. Graphical representation of the CDF of an asperity distribution and the derived function parameters S_{pk}, S_k and S_{vk}.

0 for isotropic surfaces to $|S_{mo}| = 1$ for anisotropic surfaces. The inversion of the S_{tr} parameter is required to enable the differentiation between the following situations: anisotropic texture parallel to the motion direction from anisotropic texture perpendicular to the motion direction. The second term of the equation $(\cos(2(S_{td} - \theta_{\parallel})))$ is used to control the sign of the S_{mo} parameter according to the direction of the surface texture in relation to the direction of the motion. This term results in negative values ($S_{mo} < 0$) when the texture direction is perpendicular to the motion direction and positive values ($S_{mo} > 0$) for texture direction parallel to the motion direction. Additionally, it also requires the reference angle of the motion direction, represented by the term $\theta_{\parallel}$ in Equation (1). For simplification, it's advised to measure the topography of the surfaces oriented towards the motion direction. In this case, the motion direction term is equal to zero ($\theta_{\parallel} = 0$). Otherwise, the term $\theta_{\parallel}$ needs to be used to adjust the contribution of the surface texture with respect to the motion direction.

A schematic representation of the S_{mo} for different surface conditions is shown in Fig. 6. The half-polar plot exhibits the values assumed by the proposed S_{mo} parameter for all possible combinations of the S_{tr} and S_{td} parameters. In the outer radius of the graph, which corresponds to anisotropic surfaces ($S_{tr} = 0$), the S_{mo} with higher absolute magnitudes can be found. Meanwhile, the sign of the S_{mo} parameter varies according to the S_{td} parameter. When the surface texture is parallel to the motion direction, the S_{mo} assumes positive sign ($S_{mo} > 0$). On the other hand, when the surface texture is perpendicular to the motion direction, the S_{mo} assumes negative sign ($S_{mo} < 0$). Besides, as the surface becomes more isotropic, the S_{tr} move towards the center of the polar plot and the S_{mo} assumes values close to zero. To better visualize these effects, three key surface conditions are highlighted with geometric indicators (⊥, O, ||) in Fig. 6. In the mostly negative condition (⊥), the surface is highly anisotropic ($S_{tr} = 0$) and perpendicular to the motion direction ($S_{td} = 90°$), resulting in $S_{mo} = -1$. When the surface is isotropic ($S_{tr} = 1$), represented by the "O" indicator, the orientation of the surface texture can be neglected as the value of the proposed parameter tends to zero ($S_{mo} = 0$). Finally, for the mostly positive condition (||), the surface is highly anisotropic ($S_{tr} = 0$) and parallel to the motion direction ($S_{td} = 0°$ or $180°$), resulting in $S_{mo} = +1$.

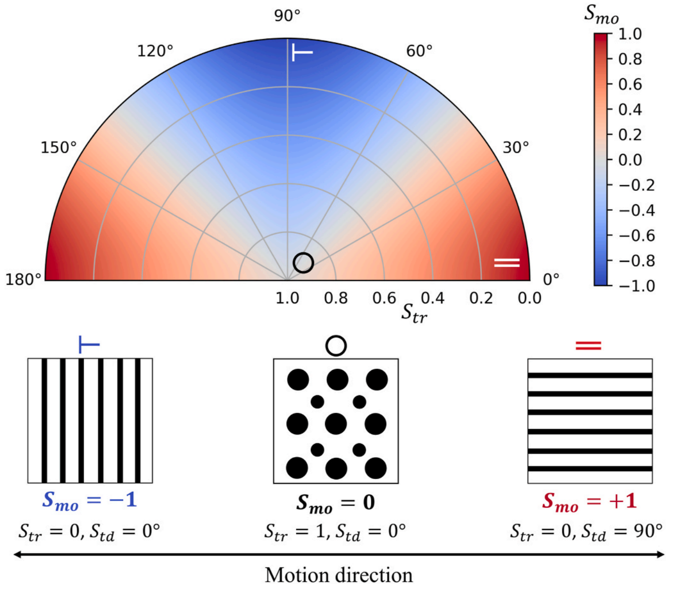

Fig. 6. Graphical representation of the surface motion orientation (S_{mo}) parameter according to the S_{tr} and S_{td} parameters and including three surface conditions.

3. Results

A typical worn surface corresponding to each of the investigated failure modes is presented in Fig. 7. It can be noticed the differences between the appearance of scuffed surfaces on one hand and the micropitting, macropitting and spalling surfaces on the other hand. The adhesive wear led to the scuffing surface seen in Fig. 7(a). This surface is evenly distributed between peaks and valleys oriented towards the motion direction. In contrast, micropitting, macropitting and spalling are all triggered by rolling contact fatigue. These surfaces exhibit a large plateau, without pronounced peaks, and with pits that form the valleys of the surface. Moreover, these pits are mostly stretched in the direction perpendicular to the motion. Lastly, an increase in the severity of the damage can be noticed, as the size and depth of the pits increase,

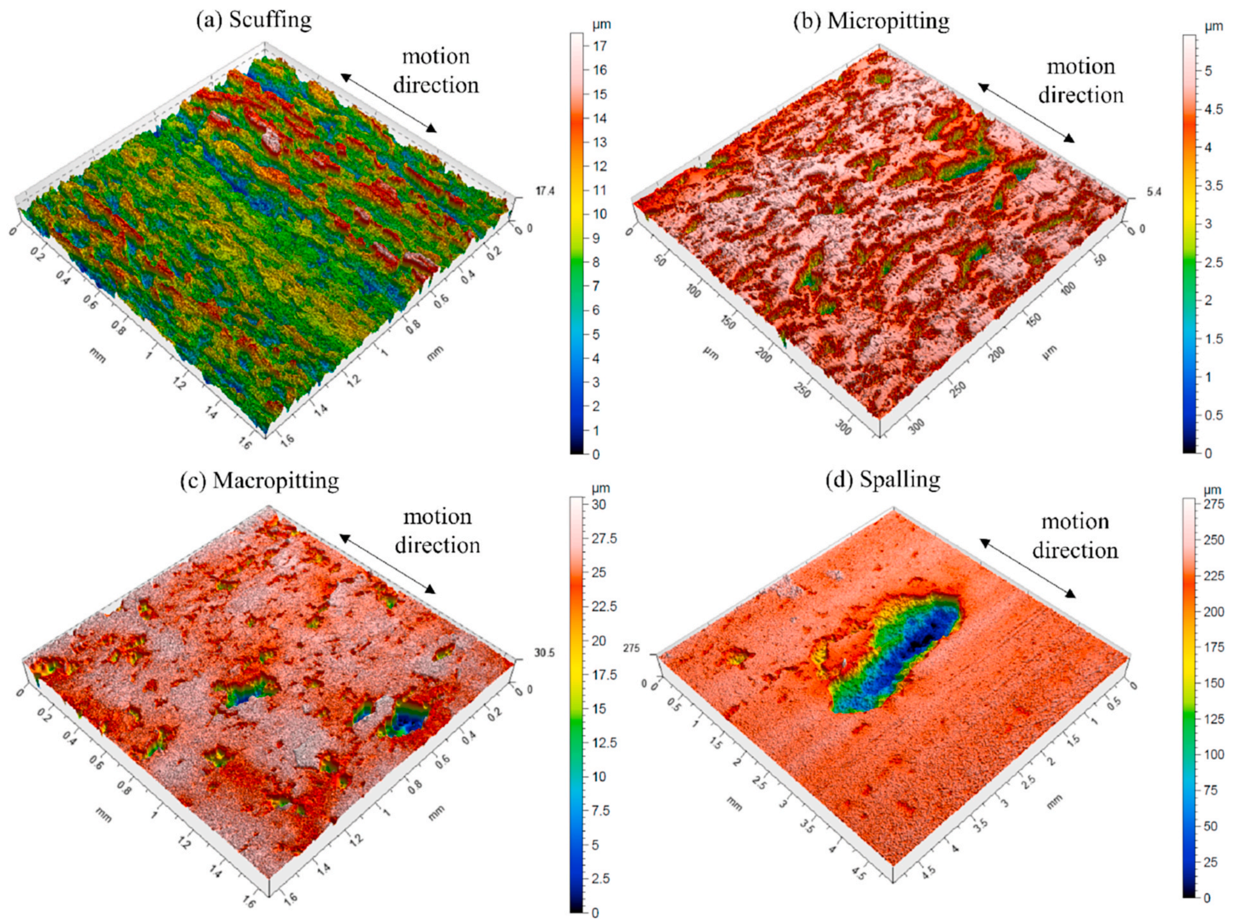

Fig. 7. Typical topography of gear failure modes: (a) scuffing, (b) micropitting, (c) macropitting, and (d) spalling.

corresponding to respectively micropitting, macropitting, and spalling.

For each gear failure mode, the average and standard deviation of the roughness parameter are enlisted in Table 3. To simplify the nomenclature, the designations *scu, mpt, pit* and *spa* were adopted in this manuscript to denote scuffing, micropitting, macropitting, and spalling failure modes, respectively. The most relevant parameters to describe the shape of the asperity distribution, the severity of the damage, and the spatial orientation of the defects are subsequently discussed in detail.

The shape of the asperities distribution can be assessed through the skewness (S_{sk}) and kurtosis (S_{ku}) parameters. Fig. 8 displays the relation found between both parameters for the evaluated surfaces. First, a clear relationship between the skewness and kurtosis can be noticed: as the surfaces are more negatively skewed, which is seen by a decrease in the S_{sk}, the flatness of the surface increases, which was measured by an increase in the S_{ku}. The same relation between these parameters had already been reported by Prajapati and Tiwari [40] in their study of rolling contact fatigue using a twin-discs test rig. Moreover, the surfaces exhibiting low kurtosis and skewness close to zero, in the bottom right corner of the graph, indicate surfaces relatively spread and symmetrically distributed between peaks and valleys. On the other hand, the surfaces exhibiting higher kurtosis and negative skewness, in the top left corner of the graph, indicate surfaces characterized by a large plateau with deep valleys. Therefore, in the current study, the skewness (S_{sk}) was selected over the kurtosis (S_{ku}) parameter, to represent the shape of the asperity distribution since it can indicate both the level and the side (peaks or valleys) to which the surface is distributed.

The average and standard deviation of the skewness parameter (S_{sk}) for each failure mode are shown in Fig. 9. In the bar plots, the error bars exhibited are equivalent to one standard deviation (±1σ). Besides, light-grey '×' markers were added to show the single measurements that resulted in the average and deviation values. Within the markers, it is

Table 3
Average (avg) and standard deviation (σ), in the format avg ± 1σ, of the evaluated roughness parameters obtained for each gear failure mode.

Roughness parameter			Gear failure mode			
Name	Symbol	Unit	scuffing (*scu*)	micropitting (*mpt*)	macropitting (*pit*)	spalling (*spa*)
skewness	S_{sk}	–	−0.08 ± 0.48	−2.54 ± 0.30	−2.82 ± 0.88	−3.66 ± 0.72
kurtosis	S_{ku}	–	3.93 ± 0.75	11.33 ± 2.82	14.23 ± 5.71	16.47 ± 6.12
root mean square height	S_q	μm	1.82 ± 0.70	0.65 ± 0.09	3.67 ± 2.13	31.74 ± 16.76
reduced peak height	S_{pk}	μm	2.16 ± 1.25	0.22 ± 0.05	1.66 ± 0.68	4.32 ± 0.52
core height	S_k	μm	4.01 ± 1.80	0.66 ± 0.07	2.81 ± 0.38	9.44 ± 0.45
reduced dale height	S_{vk}	μm	7.14 ± 1.82	4.10 ± 0.78	24.20 ± 13.21	177.71 ± 57.86
texture aspect ratio	S_{tr}	–	0.20 ± 0.10	0.47 ± 0.11	0.54 ± 0.21	0.35 ± 0.08
texture direction	S_{td}	°	89.67 ± 89.68	88.94 ± 7.12	89.69 ± 9.79	86.37 ± 0.18
surface motion orientation	S_{mo}	–	0.80 ± 0.10	−0.52 ± 0.11	−0.44 ± 0.21	−0.65 ± 0.08

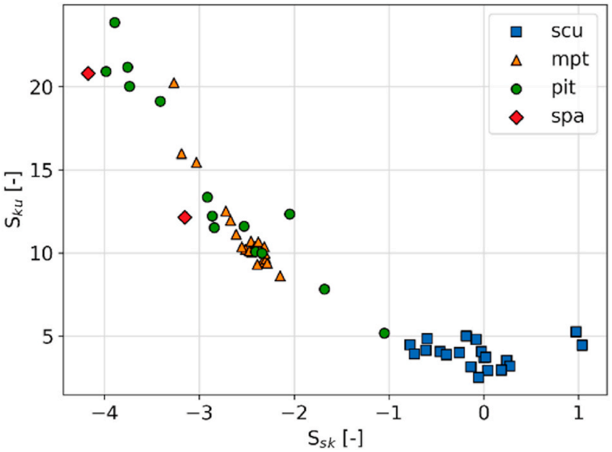

Fig. 8. Kurtosis (S_{ku}) versus Skewness (S_{sk}) of all evaluated surfaces categorized according to the failure modes.

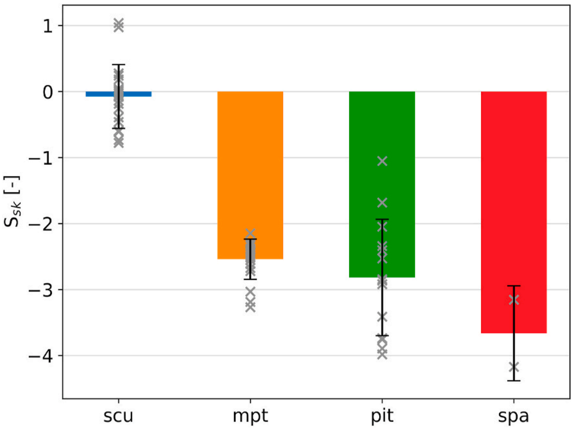

Fig. 9. Result of skewness (S_{sk}) indicating the shape of the asperity distribution for each gear failure mode.

possible to have a better idea about the distribution of the data. In Fig. 9, a clear difference is observed between scuffing and the pitting-type failures (*mpt, pit, spa*). The gear samples with scuffing failure exhibited skewness close to zero, which indicates a symmetrical distribution. This relationship of the adhesive wear leads to symmetrically distributed surfaces ($S_{sk} \cong 0$) was also reported by Gehlen et al. [43], in their investigation of the worn surfaces of polymers. In this case, the adhesive wear triggered several phenomena that can explain the current aspect of these surfaces. Due to welding, material accumulated on top of the surface, establishing the peaks. Besides, material pullout contributed to the formation of the valleys. Finally, plastic deformation may happened on top of these phenomena, contributing to the development of both peaks and valleys.

On the other hand, all fatigue-related failure modes (*mpt, pit,* and *spa*) exhibited negatively skewed asperity distributions ($S_{sk} < 0$). This can be attributed to the contact fatigue wear mechanism, which triggered the faults in the shape of pits, and consequently, established the valleys of the surfaces. Surface profiles with asymmetric distributions towards the valleys can also be seen in literature [8,13,14] in works that evaluated micropitting and pitting failures. Additionally, no significant difference was observed in the shape of the asperity distribution between these failure modes (*mpt, pit, spa*). Therefore, the shape of the asperity distribution, quantified through the skewness (S_{sk}) parameter, can differentiate the nature of the wear mechanism between adhesive or contact fatigue.

The severity of the damage can be assessed through the S_q or the function parameters (S_{pk}, S_k, S_{vk}). Fig. 10 exhibits the average and standard deviation values of the S_q parameter for each individual failure mode. A clear trend is observed in this graph, indicating an increase in the severity of damage, starting from micropitting, and subsequently followed by scuffing, macropitting, and spalling. Besides, the larger deviation of the spalling failure can be attributed to the low amount of samples considered for this failure mode.

Regarding the function parameters, Fig. 11 exhibits the average results of the function parameters (S_{pk}, S_k, S_{vk}) for each individual failure mode. In general, these parameters exhibited a similar trend to the one observed with the S_q parameter. Several authors [13–15,18,39] associated the R_{vk} parameter, which is equivalent to the S_{vk} parameter on the bidimensional approach, to the evolution of micropitting. In agreement to the literature, the S_{vk} parameter provided good discrimination between the sub-categories of fatigue failures (*mpt, pit,* and *spa*). However, the S_{vk} is a biased metric, since it only takes into account the valleys portion of the surface. The same observation is valid for the S_{pk} parameter, which takes into account only the peaks of the surface. So, the use of function parameters (S_{pk}, S_k, S_{vk}) may not be suitable for a general classification, including other types of failure modes, such as scuffing. Therefore, due to the simplicity of calculation and without prejudice to physical meaning, the S_q parameter was selected over the function parameters (S_{pk}, S_k and S_{vk}) to indicate the severity of the damage.

The results of the conventional S_{tr} and S_{td} parameters, and of the proposed S_{mo} parameter, used to identify the spatial orientation of the surface texture are described next. The average and deviation of the texture aspect ratio (S_{tr}) is shown in Fig. 12. From these results, especially considering the average values, some differentiation can be noticed between the adhesive (*scu*) and the fatigue (*mpt, pit, spa*) failure modes. The lower average of the scuffing failure ($S_{tr} = 0.20$) indicates a higher degree of anisotropy in these samples. On the other hand, the micropitting ($S_{tr} = 0.47$), pitting ($S_{tr} = 0.54$), and spalling ($S_{tr} = 0.35$) shows higher average values, which indicates that the fatigue failures resulted in more isotropic surfaces. This result was already expected since the fatigue failure is characterized by circular-shaped pits defects. Similar values ($S_{tr} = 0.35$) have been reported by Prajapati and Tiwari [40] in their assessment of micropitting. However, the fact that the fatigue failure does not result in a texture aspect ratio close to unity (S_{tr} ≈1.00) shows that the pits are not perfectly circular. Besides, based only in the S_{tr} value it is not possible to indicate the direction of the surface texture. Additionally, it is worth highlighting the existing overlap between the single results of the distinct failure modes, as shown with the light-grey '×' markers.

The results of the texture direction (S_{td}) for each failure mode are exhibited in Fig. 13. In general, no distinction can be made between the

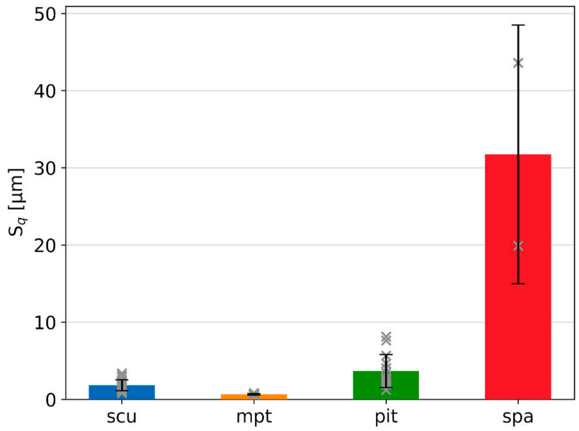

Fig. 10. Result of the S_q roughness parameter indicating the severity of damage for each gear failure mode.

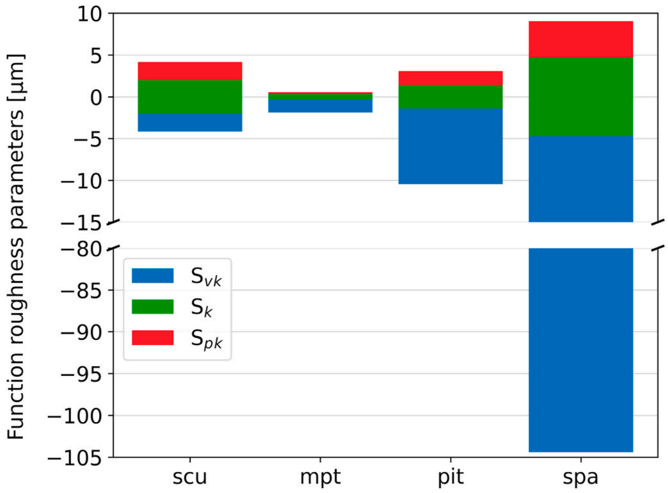

Fig. 11. Average results of the function parameters (S_{pk}, S_k, S_{vk}) for each failure mode.

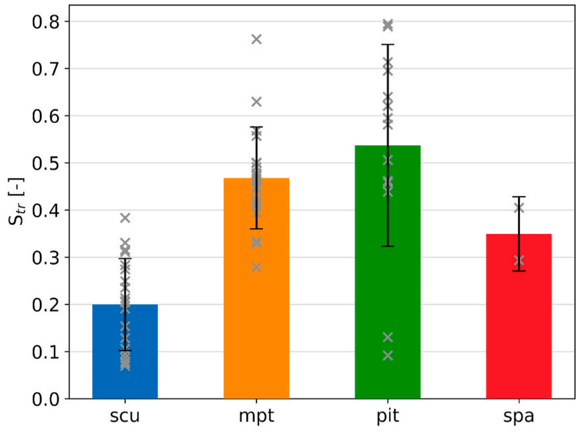

Fig. 12. Average and deviation (error bar) of the S_{tr} parameter for each failure mode.

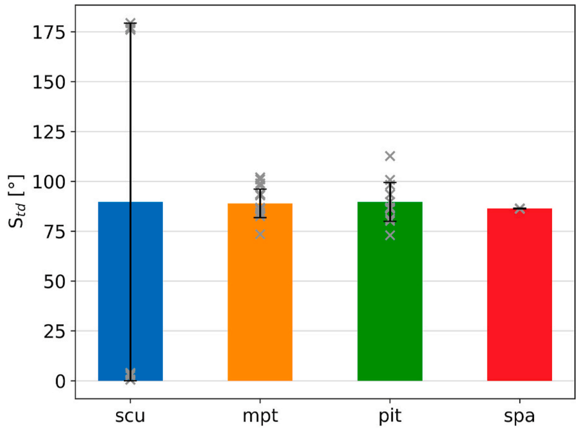

Fig. 13. Average and deviation (error bar) of the S_{td} parameter for each failure mode.

failure modes based on the average values. However, the scuffing failure showed higher deviation in comparison to the other failures. Besides, the single measurements (light-grey '×' markers) of the scuffing are located in the extremes of the parameter's range, either close to 0° or 180°. These results indicate that the direction of the scuffing phenomenon is different from the direction of the fatigue failures (*mpt, pit, spa*). In case of the scuffing failure, the direction of the anisotropy is parallel to the motion direction. Meanwhile, the direction of the anisotropy of the fatigue failures (*mpt, pit, spa*) is perpendicular to the motion direction. Therefore, the S_{td} parameter enabled the investigation of the direction of the anisotropy, which was a piece of information lacking from the analysis of the S_{tr} parameter. However, it is clear that the S_{td} parameter requires further calculations to be properly used to identify wear failure modes. For instance, an automated classification system – using the raw S_{td} data – would probably split the scuffing failure into two clusters instead of one. These considerations reinforce the necessity of a new metric, which couples the information of the S_{tr} and S_{td} parameters and provided stronger physical meaning.

Finally, the average and standard deviation of the proposed S_{mo} parameter for each failure mode is presented in Fig. 14. The scuffing exhibited, on average, a surface motion orientation of $S_{mo} = 0.8$. This value, close to the unity, indicates that the scuffing surfaces are highly anisotropic. Besides, the positive value shows that these surfaces are characterized by wear marks parallel to the rolling-sliding motion. These findings are in agreement with Martins et al. [11], who had previously stated that the roughness profile of scuffed gears highly depends on the direction in which the profilometry is performed. With the use of the proposed parameter, it was possible to quantify this relation. On the other hand, the surfaces from fatigue-induced failures (*mpt, pit, spa*) exhibited values for the surface motion orientation (S_{mo}) between -0.65 and -0.44, on average. These magnitudes indicate that there is a certain degree of anisotropy. Besides, the negative sign of the parameter ($S_{mo} < 0$) indicate that the anisotropy occurs perpendicular to the rolling-sliding motion. In this case, the pits generated by rolling contact fatigue are not perfectly circular but rather elliptical and they are elongated in the direction perpendicular to the rolling-sliding motion. This phenomenon was also observed by Brandão et al. [39], who stated that micropits are longer in the gear axial direction than in the radial direction.

In comparison to the conventional S_{tr} and S_{td} parameters, two main advantages can be highlighted from the use of the proposed S_{mo} parameter. First, it provided a better numerical distinction between adhesive and fatigue failure modes. Second, it provided a more accurate interpretation of the physical meaning, since it indicates both the strength and the direction of the surface texture with respect to the motion direction. Note, however, that it is not possible to identify significant differences between the different fatigue failures (*mpt, pit, and spa*) based on the S_{mo} value only. In summary, the orientation of the surface texture with respect to the motion direction has proven to be a suitable feature to differentiate the adhesive (*scu*) from the fatigue failures (*mpt, pit, spa*).

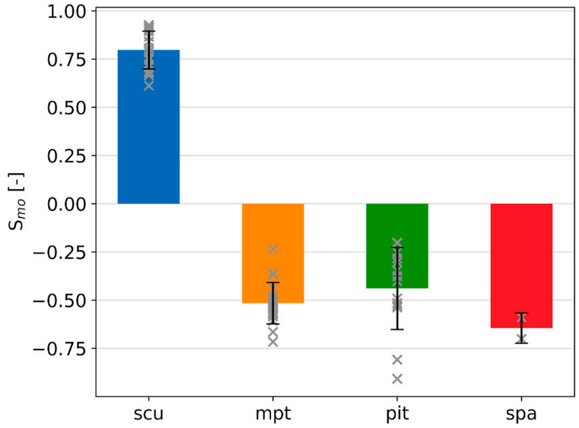

Fig. 14. Results of the proposed surface motion orientation (S_{mo}) parameter for each gear failure mode.

4. Discussion

Three features of the surface topography were identified that enable highlighting the differences between gear failure modes: the shape of the asperity distribution, the severity of the damage, and the surface texture orientation with respect to the direction of the rolling-sliding motion. In the previous section, it was shown how these features were quantified respectively by the skewness (S_{sk}), the root mean square height (S_q) and the surface motion orientation (S_{mo}) parameters. In the following section, these metrics are combined to establish an objective differentiation, and hence a classification method, between the gear failure modes.

In Fig. 15, the S_{mo} and S_{sk} parameters were plotted against each other for each evaluated surface categorized according to the respective gear failure mode (*scu, mpt, pit, or spa*). It is evident in the graph that this data can be categorized into two groups. The first group, on the top right corner of the figure (blue square marker), solely contains scuffing surfaces, exhibiting neutral skewness ($S_{sk} \cong 0$) and a strong anisotropy parallel to the motion. Meanwhile, in the bottom left corner, lie all surfaces pertaining to the fatigue failures (*mpt, pit, and spa*). These samples are featured by negative asymmetry ($S_{sk} < 0$) and a partially-anisotropic surface oriented perpendicular to the motion. Therefore, the combination of the shape of asperities distribution and the spatial orientation can successfully differentiate the scuffing failure, triggered by adhesive wear, from the failure modes originated by contact fatigue (*mpt, pit, spa*).

The severity of damage is a third feature required to further differentiate the gear failure modes. Hence, the behavior of the S_q parameter against the S_{sk} and S_{mo} parameters is shown in Fig. 16. Since only two spalling instances were found, they were omitted from Fig. 16 to provide better visual discrimination between the other surface phenomena. In fact, these spalling surfaces exhibited S_q values at least twice as higher as of any other surface in the dataset. To support the analysis from Fig. 16, top-view images of the surfaces with the lowest and the highest S_q values are shown in Figs. 17, 18 and 19, for the scuffing, micropitting, and macropitting failure modes, respectively. The numbers of these figures were added to the respective point in Fig. 16 to indicate the addressed surface.

In Fig. 16, the surfaces from scuffing failure are relatively gathered on the right side of the graphs, especially in Fig. 16b, where a more compacted group can be seen. Additionally, it can be noted that the surfaces from this gear set cover different severities of the scuffing failure. First, the scuffing surface of the smaller value of S_q (Fig. 17a) exhibits a mild form of scuffing wear. On the other hand, the surface with the larger S_q value of this set (Fig. 17b) exhibits a more severe failure mode, with formation of patches on the surface, which is a typical aspect of the plastic deformation promoted by the adhesive wear mechanism.

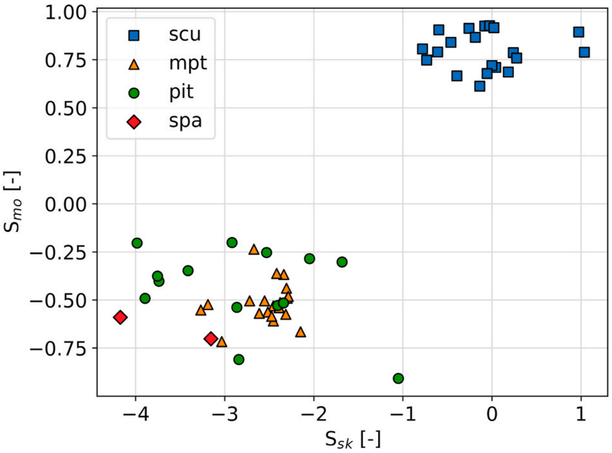

Fig. 15. Distribution of the surface motion orientation (S_{mo}) versus the skewness (S_{sk}) parameters.

Regarding the micropitted surfaces in Fig. 16, they are located in a tight group at negative values of S_{mo} and S_{sk}, and small values of S_q. This implies that there is not much variation in the roughness amplitude and hence the severity of this failure mode. This was confirmed by the similarities in the amplitude ranges of the surfaces exhibited in Fig. 18a and Fig. 18b, corresponding to the smallest and the largest S_q values obtained for this failure mode. In contrast to the micropitted surfaces, the macropitted surfaces, although also located at negative values of S_{mo} and S_{sk} in Fig. 16, presented much larger values of S_q and with a larger variation. Indeed, as shown in Fig. 19, the pitting set includes surfaces with small pits (Fig. 19a), to surfaces with large and deep pits (Fig. 19b).

Moreover, Fig. 16 shows that micropitted surfaces typically display $S_q \leq 1\mu m$. This suggests the existence of a threshold of $S_q = 1\mu m$, that potentially serves as a differentiator between micropitting and macropitting. From the literature [12–14,16], a single micropit is defined as having a few micrometers wide and up to 20 μm deep, which requires the prior identification of each pit in order to evaluate its size. Therefore, the use of an overall metric of the surface roughness, such as the S_q parameter, can facilitate the differentiation between micropitting and other failure modes, like macropitting. However, three limitations have to be considered regarding this result. First, the micropitting set evaluated in this work exhibited pit depths of 5 μm, without larger variations, as seen mentioned in the analysis of Fig. 18, which suggests that the threshold ($S_q = 1\mu m$) can be higher if deeper micropits (up to 20 μm deep) are measured. Second, it cannot be implied that gears subjected to pitting tests cannot develop micropitting besides macropitting. For instance, on the damaged gear surface that exhibited the smallest S_q, as shown in Fig. 19a, it is possible to identify small pits consistent with the definition of micropitting. Third, it is more reasonable to consider that there is a range of S_q values with overlapping of the micropitting and the macropitting phenomena. Above this range, the surfaces predominantly exhibit macropitting and the effects of micropitting can be safely neglected, as seen in the surface of Fig. 19b. Therefore, further investigations have to be conducted to fully determine this range.

Additionally, due to the similarity between the graphs of $S_q \times S_{sk}$ (Fig. 16a) and $S_q \times S_{mo}$ (Fig. 16b), it may raise a valid claim that using the severity of damage parameter (S_q) associated to only one of the other parameters (S_{sk} or S_{mo}) is enough to distinguish between the gear failure modes. Indeed, this is valid for the surfaces evaluated in this study, especially if it is considered the parameters S_q and S_{mo}, exhibited in Fig. 16b. Nevertheless, the skewness (S_{sk}) and the surface motion orientation (S_{mo}) parameters hold completely different physical meanings. The first (S_{sk}) indicates how the surface is distributed alongside the height, without considering the spatial orientation. The second (S_{mo}), on the other hand, only shows how the damage defects are oriented over the surface. For instance, the collective consideration of these three features should be relevant for the identification of failure modes not included in this investigation, such as abrasion. Therefore, the authors herein support the argument that all three indicators (S_q, S_{sk}, S_{mo}) are equally important for the identification of gear failure modes.

5. Conclusions

In the current study, the surface topography of gears containing different failure modes (micropitting, pitting, and scuffing) was evaluated in terms of roughness parameters. These roughness parameters were combined to provide an objective classification of the gear failure modes. The following set of conclusions could be stated:

- The surfaces with distinct failure modes exhibited significant differences in three features: the shape of asperities distribution, the severity of damage and surface texture orientation with respect to the motion direction;

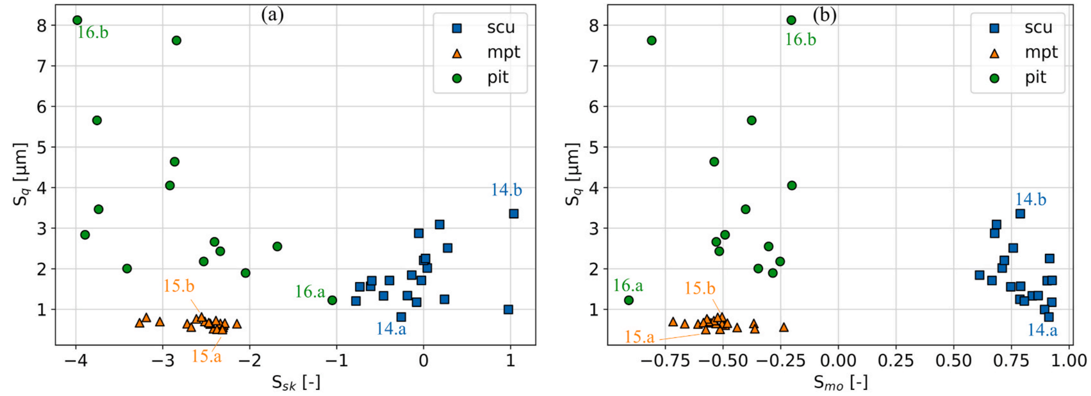

Fig. 16. Distribution of the severity of damage (S_q) parameter against the S_{sk} (a) and the S_{mo} (b) parameters for the surfaces of the *mpt, pit, and scu* failure modes, the colored numbers indicate the figure with the image of respective the surface.

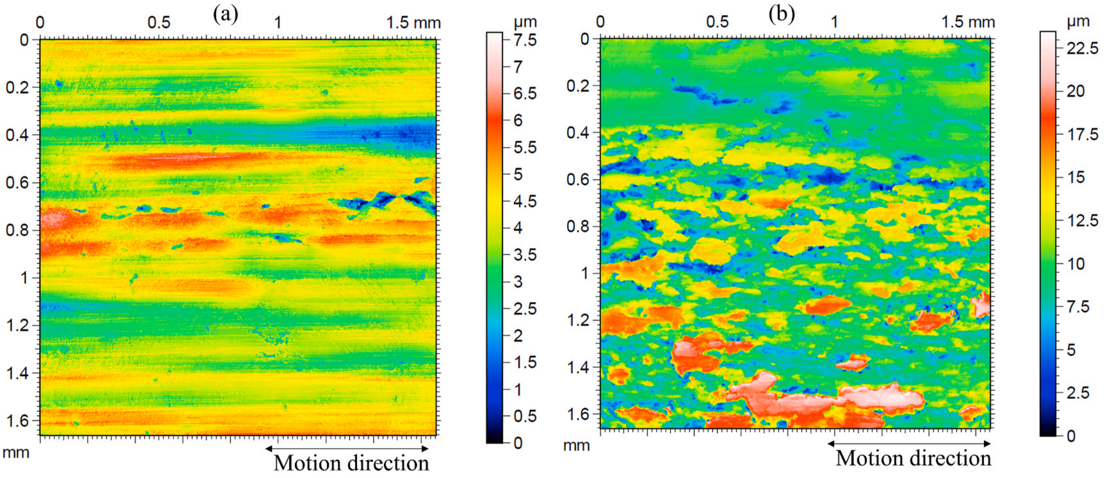

Fig. 17. Top view images of the gear surfaces with the lowest (a) and the highest (b) severity of damage from the scuffing failure mode.

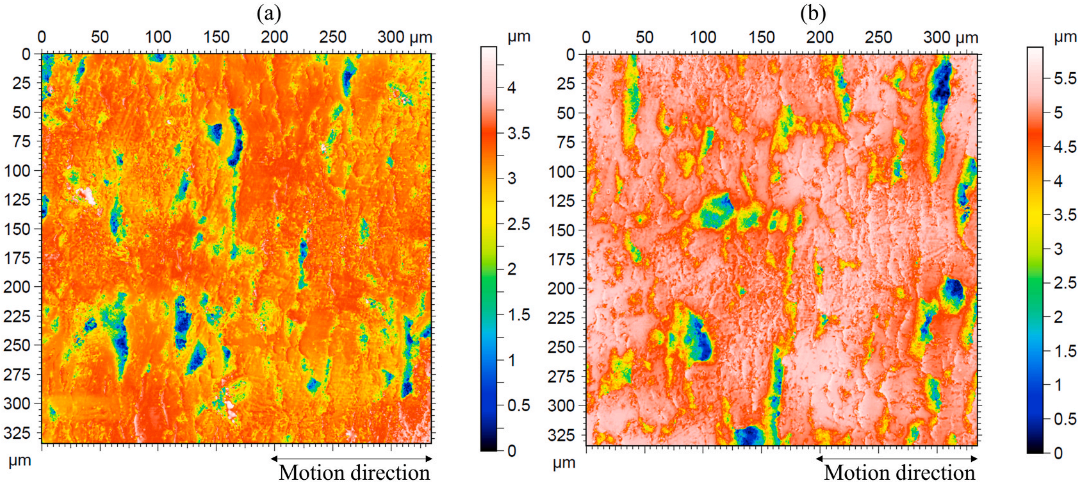

Fig. 18. Top view images of the gear surfaces with the lowest (a) and the highest (b) severity of damage from the micropitting failure mode.

- The skewness (S_{sk}) parameter is suitable to quantify the shape of the asperity distribution;
- The root mean square height (S_q) parameter is suitable to quantify the severity of damage;
- A new roughness parameter was proposed: surface motion orientation (S_{mo});
- The S_{mo} parameter is suitable to quantify the surface texture orientation with respect to the motion direction;
- The S_{sk} and S_{mo} parameters were used to distinguish between failure modes originating from the adhesive wear (scuffing) to those triggered by the contact fatigue wear mechanism (micropitting, macropitting and spalling);

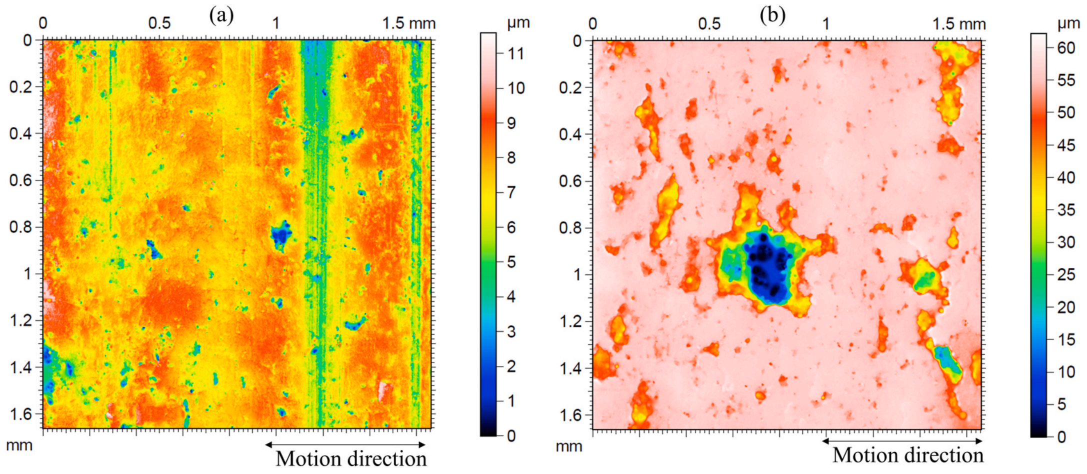

Fig. 19. Top view images of the gear surfaces with the lowest (a) and the highest (b) severity of damage from the pitting failure mode.

- The S_q parameter enabled the identification of different levels of severity of damage and the further classification of the scuffing, micropitting, and macropitting failure modes.

The conclusions presented herein are limited to the scope of this work. Further verifications are encouraged to verify the extent of the current results in gear systems subjected to different experimental setups and operating conditions. For a future perspective, the authors intend to extend the current gear topography dataset, both in the number of surfaces and in the types of different gear failure modes. For instance, it will enable a deeper investigation of the S_q thresholding, which has shown to be promising to differentiate the severity of damage between the pitting failure modes (micropitting, macropitting and spalling). Moreover, this would allow the application of machine learning techniques, and the development of an automated system for gear failure mode identification, based on roughness parameters.

CRediT authorship contribution statement

J.C. Poletto: Conceptualization, Methodology, Formal Analysis, Investigation, Writing - Original Draft. **C.M.C.G. Fernandes:** Conceptualization, Resources. **L.Y. Barros:** Formal Analysis, Writing - Review & Editing. **P.D. Neis:** Supervision, Writing - Review & Editing. **K. Pondicherry:** Investigation, Writing - Review & Editing. **D. Fauconnier:** Supervision, Methodology, Writing - Review & Editing. **J.H.O. Seabra:** Resources. **P. De Baets:** Supervision. **N.F. Ferreira:** Conceptualization, Supervision.

Declaration of competing interest

The authors declare that they have no known competing financial interests or personal relationships that could have appeared to influence the work reported in this paper.

Acknowledgments

This study was financed in part by the Coordenação de Aperfeiçoamento de Pessoal de Nível Superior – Brasil (CAPES) – Finance Code 001 and by the Conselho Nacional de Desenvolvimento Científico e Tecnológico – Brasil (CNPq). Carlos M. C. G. Fernandes and Jorge H.O. Seabra are grateful for the funding through LAETA, Portugal in the framework of project UID/50022/2020.

References

[1] P. Krajnik, F. Hashimoto, B. Karpuschewski, E.J. da Silva, D. Axinte, Grinding and fine finishing of future automotive powertrain components, CIRP Ann 70 (2021) 589–610, https://doi.org/10.1016/j.cirp.2021.05.002.
[2] W. Feng, Z. Feng, L. Mao, Failure analysis of a secondary driving helical gear in transmission of electric vehicle, Eng. Fail. Anal. 117 (2020), 104934, https://doi.org/10.1016/j.engfailanal.2020.104934.
[3] X. Chen, J. Hong, Y. Wang, Y. Ma, Fatigue failure analysis of the central-driven bevel gear in a turboshaft engine arising from multi-source excitation, Eng. Fail. Anal. 119 (2021), 104811, https://doi.org/10.1016/j.engfailanal.2020.104811.
[4] C. Dao, B. Kazemtabrizi, C. Crabtree, Wind turbine reliability data review and impacts on levelised cost of energy, Wind Energy 22 (2019) 1848–1871, https://doi.org/10.1002/we.2404.
[5] L. Xiang, C. An, Y. Zhang, A. Hu, Failure dynamic modelling and analysis of planetary gearbox considering gear tooth spalling, Eng. Fail. Anal. 125 (2021), 105444, https://doi.org/10.1016/j.engfailanal.2021.105444.
[6] J. Lin, H. Li, P. Wang, N. Li, Z. Shi, U. Olofsson, Compensation of mounting error in in-situ wear measurement during gear pitting test, Meas. J. Int. Meas. Confed. 191 (2022), 110808, https://doi.org/10.1016/j.measurement.2022.110808.
[7] J. Kattelus, J. Miettinen, A. Lehtovaara, Detection of gear pitting failure progression with on-line particle monitoring, Tribol. Int. 118 (2018) 458–464, https://doi.org/10.1016/j.triboint.2017.02.045.
[8] J. Lin, C. Teng, E. Bergstedt, H. Li, Z. Shi, U. Olofsson, A quantitatively distributed wear-measurement method for spur gears during micro-pitting and pitting tests, Tribol. Int. 157 (2021), 106839, https://doi.org/10.1016/j.triboint.2020.106839.
[9] E. Bergstedt, J. Lin, U. Olofsson, Influence of gear surface roughness on the pitting and micropitting life, Proc. Inst. Mech. Eng. Part C J. Mech. Eng. Sci. 234 (2020) 4953–4961, https://doi.org/10.1177/0954406220931541.
[10] B.R. Höhn, K. Michaelis, Influence of oil temperature on gear failures, Tribol. Int. 37 (2004) 103–109, https://doi.org/10.1016/S0301-679X(03)00047-1.
[11] R. Martins, N. Cardoso, J. Seabra, Influence of lubricant type in gear scuffing, Ind. Lubric. Tribol. 60 (2008) 299–308, https://doi.org/10.1108/00368790810918695.
[12] ISO 10825, Gears — wear and damage to gear teeth — terminology, Int. Organ. Stand. (2021).
[13] N.F.R. Cardoso, R.C. Martins, J.H.O. Seabra, A. Igartua, J.C. Rodríguez, R. Luther, Micropitting performance of nitrided steel gears lubricated with mineral and ester oils, Tribol. Int. 42 (2009) 77–87, https://doi.org/10.1016/j.triboint.2008.05.010.
[14] N.F.R. Cardoso, R.C. Martins, J.H.O. Seabra, Micropitting of carburized gears lubricated with biodegradable low-toxicity oils, Proc. Inst. Mech. Eng. Part J J. Eng. Tribol. 223 (2009) 481–495, https://doi.org/10.1243/13506501JET495.
[15] R. Martins, C. Locatelli, J. Seabra, Evolution of tooth flank roughness during gear micropitting tests, Ind. Lubric. Tribol. 63 (2011) 34–45, https://doi.org/10.1108/00368791111101821.
[16] F. Antoine, J. Besson, Simplified modellization of gear micropitting, Proc. Inst. Mech. Eng. Part G J. Aerosp. Eng. 216 (2002) 291–302, https://doi.org/10.1243/095441002321029035.
[17] V. Moorthy, B.A. Shaw, Contact fatigue performance of helical gears with surface coatings, Wear 276–277 (2012) 130–140, https://doi.org/10.1016/j.wear.2011.12.011.
[18] R. Martins, J. Seabra, L. Magalhães, Austempered ductile iron (ADI) gears: power loss, pitting and micropitting, Wear 264 (2008) 838–849, https://doi.org/10.1016/j.wear.2007.05.007.
[19] H. Liu, H. Liu, C. Zhu, A Review on Micropitting Studies of Steel Gears, 2019, pp. 1–27, https://doi.org/10.3390/coatings9010042.
[20] H. Chang, P. Borghesani, W.A. Smith, Z. Peng, Application of surface replication combined with image analysis to investigate wear evolution on gear teeth – a case study, Wear 430–431 (2019) 355–368, https://doi.org/10.1016/j.wear.2019.05.024.

[21] Y. Ding, N.F. Rieger, Spalling formation mechanism for gears, Wear 254 (2003) 1307–1317, https://doi.org/10.1016/S0043-1648(03)00126-1.

[22] H. Chang, P. Borghesani, Z. Peng, Automated assessment of gear wear mechanism and severity using mould images and convolutional neural networks, Tribol. Int. 147 (2020), 106280, https://doi.org/10.1016/j.triboint.2020.106280.

[23] C. Gonzalez-Arias, C.C. Viafara, J.J. Coronado, F. Martinez, Automatic classification of severe and mild wear in worn surface images using histograms of oriented gradients as descriptor, Wear 426–427 (2019) 1702–1711, https://doi.org/10.1016/j.wear.2018.11.028.

[24] M. Wolski, T. Woloszynski, P. Podsiadlo, G.W. Stachowiak, En route to the automated wear surface classification system : differentiating between adhesive , abrasive , and corrosive wear under different load conditions, Tribol. Lett. 68 (2020) 1–12, https://doi.org/10.1007/s11249-020-01326-5.

[25] P.M. Sieberg, D. Kurtulan, S. Hanke, Wear mechanism classification using artificial intelligence, Materials 15 (2022) 2358, https://doi.org/10.3390/ma15072358.

[26] ISO 25178-2, Geometrical product specifications (GPS) — surface texture: areal Part 2: terms, definitions and surface texture parameters, Int. Organ. Stand. (2012).

[27] ISO 14635-1, Gears - FZG test procedures - Part 1: FZG test method A/8.3/90 for relative scuffing load-carrying capacity of oils, Int. Organ. Stand. (2000).

[28] FZG Gear Research Centre of the Technical University Munich, Short Test Procedure for the Investigation of the Micro-pitting Load Capacity of Gear Lubricants, DGMK-FZG Micro-Pitting Short Test, 2002.

[29] FZG Gear Research Centre of the Technical University Munich, Short test procedure to investigate the lubricant influence on the pitting carrying capacity of gears, DGMK-FZG Short Durat. Pitting Test. (2006).

[30] J. Castro, J. Seabra, Scuffing and lubricant film breakdown in FZG gears part I. Analytical and experimental approach, Wear 215 (1998) 104–113, https://doi.org/10.1016/S0043-1648(97)00277-9.

[31] M. Sosa, S. Björklund, U. Sellgren, U. Olofsson, In situ surface characterization of running-in of involute gears, Wear 340–341 (2015) 41–46, https://doi.org/10.1016/j.wear.2015.03.008.

[32] Q. Qi, T. Li, P.J. Scott, X. Jiang, A correlational study of areal surface texture parameters on some typical machined surfaces, Procedia CIRP 27 (2015) 149–154, https://doi.org/10.1016/j.procir.2015.04.058.

[33] W.P. Dong, P.J. Sullivan, K.J. Stout, Comprehensive study of parameters for characterising three- dimensional surface topography. III: parameters for characterising amplitude and some functional properties, Wear 178 (1994) 29–43, https://doi.org/10.1016/0043-1648(94)90127-9.

[34] M. Sedlaček, B. Podgornik, J. Vižintin, Influence of surface preparation on roughness parameters, friction and wear, Wear 266 (2009) 482–487, https://doi.org/10.1016/j.wear.2008.04.017.

[35] M. Stewart, A new approach to the use of bearing area curve, Soc. Manuf. Eng. (1990) FC90–229.

[36] S. Zhu, P. Huang, Influence mechanism of morphological parameters on tribological behaviors based on bearing ratio curve, Tribol. Int. 109 (2017) 10–18, https://doi.org/10.1016/j.triboint.2016.12.014.

[37] B.G. Rosén, R. Ohlsson, T.R. Thomas, Wear of cylinder bore microtopography, Wear 198 (1996) 271–279, https://doi.org/10.1016/0043-1648(96)07207-9.

[38] R. Leach, Characterisation of Areal Surface Texture, Springer Berlin Heidelberg, Berlin, Heidelberg, 2013, https://doi.org/10.1007/978-3-642-36458-7.

[39] J.A. Brandão, J.H.O. Seabra, J. Castro, Surface initiated tooth flank damage. Part II: prediction of micropitting initiation and mass loss, Wear 268 (2010) 13–22, https://doi.org/10.1016/j.wear.2009.07.020.

[40] D.K. Prajapati, M. Tiwari, Experimental investigation on evolution of surface damage and topography parameters during rolling contact fatigue tests, Fatig. Fract. Eng. Mater. Struct. 43 (2020) 355–370, https://doi.org/10.1111/ffe.13150.

[41] L. Blunt, X. Jiang, Advanced Techniques for Assessment Surface Topography: Development of a Basis for 3D Surface Texture Standards "Surfstand,", 2003. London.

[42] W. Grabon, P. Pawlus, Description of two-process surface topography, Surf. Topogr. Metrol. Prop. 2 (2014), https://doi.org/10.1088/2051-672X/2/2/025007.

[43] G.S. Gehlen, P.D. Neis, J.C. Poletto, L.Y. Barros, D. Buneder, N.F. Ferreira, Pressure-velocity limit evaluation on POM-C + carbon black at different temperatures, Wear 464–465 (2021), 203530, https://doi.org/10.1016/j.wear.2020.203530.